J. Fluid Mech. (1989), *vol.* 201, *pp.* 299–322
Printed in Great Britain

Models for very wide-angle water waves and wave diffraction. Part 2. Irregular bathymetry

By ROBERT A. DALRYMPLE†, KYUNG DUCK SUH†, JAMES T. KIRBY‡ AND JANG WON CHAE§

† Ocean Engineering Group, Department of Civil Engineering, University of Delaware, Newark, DE 19716, USA

‡ Coastal and Oceanographic Engineering Department, University of Florida, Gainesville, FL 32611, USA

§ Ocean Engineering Laboratory, Korea Ocean Research and Development Institute, P.O. Box 29, Panwol Ind., Ansan, 171-14, Korea

(Received 29 January 1988)

A wide-angle model for water-wave propagation on an irregular bathymetry is developed based on the linear mild-slope equation. The spectral model decomposes the incident wavetrain into directional modes, or an angular spectrum. The effect of the bottom topography is shown to force the generation of additional directional wave modes. Nonlinearity is incorporated in the model by correcting the wave parameters iteratively using an empirical nonlinear dispersion relationship which is approximately valid over the entire range of water depths.

Numerical examples are presented for waves incident on a transverse bar field, a laboratory experiment involving wave focusing over an elliptic shoal on a sloping beach for which detailed measurements are available and for waves focusing behind a circular shoal resting on a flat bottom. The application of the model is limited to cases in which the model domain is rectangular and the depth variation in the lateral direction is small if waves of large incident angle are modelled.

1. Introduction

For the past decade, the parabolic-equation method has been one of the various methods used to model the propagation of surface waves over water of varying depths. The analysis by Liu & Mei (1976) was one of the first parabolic treatments of this problem. The development of the mild-slope equation (Berkhoff 1972) and its parabolic representation by Radder (1979), and the subsequent development of nonlinear versions of this equation by Kirby & Dalrymple (1983) and Liu & Tsay (1984) allowed the generation of numerical models which could predict the evolution of monochromatic waves in coastal regions reasonably well. There is a significant drawback of the parabolic method, however, in that it requires that the waves propagate nearly along a given direction (positive x-direction in this paper). Deviations of the wave direction, due to refraction and diffraction, away from this direction lead to errors, which are usually small for waves propagating in directions not greater than 30° from the x-direction. Other methods such as finite-element solutions of the mild-slope equation, e.g. Berkhoff (1972), do not have this angular restriction, and can solve for the full wave field including the back-scattered wave, which is neglected in most of the available parabolic models. However, the parabolic-

equation method is computationally more convenient and rapid than other methods, and as mentioned can incorporate nonlinearity in a rigorous fashion.

Efforts towards developing a wide-angle parabolic model have been made, e.g. Booij (1981) and Kirby (1986*a*, *b*). Very recently Dalrymple & Kirby (1988) have developed a wave propagation model valid for angles of propagation up to 90°, based on the assumption that the bottom contours were straight and parallel in a direction normal to the assumed propagation direction. Their analysis showed that the wave field can be decomposed into an angular spectrum, that is, the superposition of many synchronous wavetrains propagating at different angles to the x-axis, varying from 0 to $\pm\pi/2$ radians. (An angular spectrum model has been used previously on constant depth by Stamnes *et al.* 1983.) Dalrymple & Kirby pointed out that for problems such as wave diffraction through a breakwater gap the diffraction pattern observed behind the gap is fixed by the initial condition at the gap. The wave pattern behind the gap is simply the radial spreading of the initial angular spectrum, each directional mode of which simply refracts and shoals.

In the present study, we extend the Dalrymple & Kirby's model to the case of irregular bathymetry, relaxing the straight and parallel contours assumption, which permits us to examine situations where diffraction occurs within the model domain. In §2 our wide-angle model for an irregular bathymetry is derived through the use of Fourier decomposition which produces a convolution term involving interaction between the bottom and the wave modes. In §3 the approximation of the problem in the discrete Fourier space and the numerical method are described. The conditions for stability and accuracy of the numerical method are also discussed. Section 4 illustrates the incorporation of nonlinearity in the model. In §5 the mechanism for the evolution of directional wave modes due to the interaction between surface wave and bottom topography is examined. In §§6 and 7 numerical examples are presented to show the validity of the model for an irregular bathymetry and a large angle of incidence, respectively, and finally in §8 some restrictions on the model are discussed.

2. Governing equation and Fourier decomposition

In order to study the combined refraction and diffraction of waves, the governing equation is taken to be the linear mild-slope equation developed by Berkhoff (1972), which has been used in the water-wave propagation models of Radder (1979), Booij (1981), and Dingemans *et al.* (1984):

$$\nabla\cdot(CC_g\nabla\Phi)+k^2CC_g\Phi=0, \tag{1}$$

where ∇ is a gradient operator in horizontal coordinates (x, y), $k(x, y)$ is the local wavenumber, C and C_g are the local phase and group velocities, respectively, and $\Phi(x, y)$ is the horizontal spatial variation of the wave potential and is directly related to the free-surface elevation of the wave. The total velocity potential for the wave motion is

$$\Phi' = \mathrm{i}\Phi\frac{g\cosh k(h+z)}{\omega\cosh kh}\mathrm{e}^{-\mathrm{i}\omega t}. \tag{2}$$

The vertical coordinate z is measured vertically upwards from the still water line. The wavenumber k must satisfy the dispersion relationship, which relates k to the wave angular frequency ω and the water depth $h(x, y)$ by

$$\omega^2 = gk\tanh kh, \tag{3}$$

where g is the gravitational acceleration. This relation will be modified later to incorporate nonlinearity in the model.

Using the definitions of $p(x,y) = CC_g$ and $\phi = p^{\frac{1}{2}}\Phi$, the mild-slope equation becomes (Radder 1979)

$$\nabla^2\phi + k_c^2\phi = 0, \tag{4}$$

where

$$k_c^2 = k^2 - \frac{\nabla^2 p^{\frac{1}{2}}}{p^{\frac{1}{2}}}. \tag{5}$$

The Helmholtz equation (4) forms the basis of Radder's parabolic approximation. For later convenience, we define a laterally averaged wavenumber, $\bar{k}$, as

$$\bar{k}^2 = \frac{1}{l}\int_0^l k_c^2 \,\mathrm{d}y \tag{6}$$

so that

$$k_c^2 = \bar{k}^2(1-\nu^2), \tag{7}$$

where

$$\nu^2 = 1 - \frac{k_c^2}{\bar{k}^2}, \tag{8}$$

and l is the width of the model area in the y-direction. Note that $\bar{k}^2$ is a function of x only and the variability of depth in the y-direction is contained in $\nu^2(x,y)$, whose magnitude is usually much smaller than unity if the topography does not deviate drastically from straight and parallel contours. Substituting (7) into (4) gives

$$\nabla^2\phi + \bar{k}^2\phi - \bar{k}^2\nu^2\phi = 0. \tag{9}$$

The last term on the left-hand side allows for the effects of the depth variability in the y-direction.

The Fourier transform of (9) in the y-direction leads to the decomposition of the potential into modes:

$$\hat{\phi}_{xx} + (\bar{k}^2 - \lambda^2)\hat{\phi} - \bar{k}^2 F(\nu^2\phi) = 0, \tag{10}$$

where the caret denotes a variable in the Fourier space, λ is the continuous Fourier parameter, $F(\ )$ denotes the Fourier transform, and the subscript x denotes differentiation. Note that the Fourier transform of $(\nu^2\phi)$ involves ϕ in the real space. Following Dalrymple & Kirby (1988), this equation is split, in the Fourier space, into two first-order equations by assuming

$$\hat{\phi}(x,\lambda) = \hat{\phi}^+ + \hat{\phi}^- \quad (\text{and } \phi(x,y) = \phi^+ + \phi^-), \tag{11}$$

where the superscripts + and − denote the forward-propagating and back-scattered potentials, respectively. Further we assume that we can split (11) into the following forms:

$$\hat{\phi}_x^+ = \mathrm{i}(\bar{k}^2 - \lambda^2)^{\frac{1}{2}}\hat{\phi}^+ + G(x,\lambda), \tag{12}$$

$$\hat{\phi}_x^- = -\mathrm{i}(\bar{k}^2 - \lambda^2)^{\frac{1}{2}}\hat{\phi}^- - G(x,\lambda), \tag{13}$$

where $G(x,\lambda)$ is an unknown function which is included to resolve the x-dependency of $\bar{k}^2$. Substituting these expressions into (10) gives

$$G(x,\lambda) = \frac{-\mathrm{i}[\bar{k}^2 - \lambda^2]_x^{\frac{1}{2}}(\hat{\phi}^+ - \hat{\phi}^-) + \bar{k}^2 F[\nu^2(\phi^+ + \phi^-)]}{2\mathrm{i}(\bar{k}^2 - \lambda^2)^{\frac{1}{2}}}. \tag{14}$$

By neglecting the assumed small back-scattered wave, the propagation model for the forward-propagating wave is obtained:

$$\hat{\phi}^+_x = \mathrm{i}(\bar{k}^2-\lambda^2)^{\frac{1}{2}}\hat{\phi}^+ - \frac{[\bar{k}^2-\lambda^2]^{\frac{1}{2}}_x}{2(\bar{k}^2-\lambda^2)^{\frac{1}{2}}}\hat{\phi}^+ - \frac{\mathrm{i}\bar{k}^2 F(\nu^2\phi^+)}{2(\bar{k}^2-\lambda^2)^{\frac{1}{2}}}, \tag{15}$$

where $\bar{k}$ and λ are now understood as the wavenumber in the propagation direction and its projection in the y-direction, respectively. Then $(\bar{k}^2-\lambda^2)^{\frac{1}{2}}$ represents the projection of the wavenumber in the x-direction. As λ exceeds $\bar{k}$ in magnitude, the wavenumber in the x-direction becomes imaginary, indicating evanescent modes which decay exponentially in the x-direction.

The second term on the right-hand side of (15) represents the shoaling/refraction of each wave mode. The $F(\nu^2\phi^+)$ term represents the interaction between surface wave and the lateral bottom variation, which will be examined in detail later. For straight and parallel bottom contours, Dalrymple & Kirby's (1988) equation results.

3. Numerical method and stability analysis

Equation (15), with a proper initial condition at $x = 0$, can be solved by a spectral Fourier method which imposes periodic lateral boundary conditions in the y-direction. These conditions frequently are not met in many applications, so in such cases the lateral extent of the model domain should be taken large enough so that the boundaries do not affect the area being studied. In the spectral Fourier method, the domain is discretized in the y-direction by N equidistant points, with spacing $\Delta y = l/(N-1)$. The velocity potential $\phi^+(x,y)$, numerically defined only on these points, can be transformed into discrete Fourier modes by

$$\hat{\phi}^+(x,n) = \frac{1}{N}\sum_{j=0}^{N-1}\phi^+(x,j\Delta y)\,\mathrm{e}^{-\mathrm{i}n\lambda j\Delta y}, \quad n = 0, \pm1, \pm2, \ldots, \pm(\tfrac{1}{2}N-1), -\tfrac{1}{2}N. \tag{16}$$

The inversion formula is

$$\phi^+(x,j\Delta y) = \sum_n \hat{\phi}^+(x,n)\,\mathrm{e}^{\mathrm{i}n\lambda j\Delta y}, \quad j = 0, 1, 2, \ldots, (N-1), \tag{17}$$

where

$$\lambda = \frac{2\pi}{N\Delta y}, \tag{18}$$

which is different from the continuous Fourier parameter λ used in the previous section. Subsequently, λ is defined by (18). These transforms can be performed efficiently by using a fast Fourier transform (FFT).

In the discrete Fourier space, (15) can be approximated by

$$\left.\begin{aligned}\hat{\phi}^+_x = \mathrm{i}(\bar{k}^2-(n\lambda)^2)^{\frac{1}{2}}\hat{\phi}^+ - \frac{[\bar{k}^2-(n\lambda)^2]^{\frac{1}{2}}_x}{2[\bar{k}^2-(n\lambda)^2]^{\frac{1}{2}}}\hat{\phi}^+ - \frac{\mathrm{i}\bar{k}^2 F_n(\nu^2\phi^+)}{2[\bar{k}^2-(n\lambda)^2]^{\frac{1}{2}}},\\ n = 0, \pm1, \pm2, \ldots, \pm(\tfrac{1}{2}N-1), -\tfrac{1}{2}N,\end{aligned}\right\} \tag{19}$$

where F_n denotes the nth component of the discrete Fourier transform. The initial conditions, $\hat{\phi}^+(0,n)$, are obtained by using the FFT on the discretized values of $\phi^+(0,j\Delta y), j = 0$ to $(N-1)$. The numerical procedure involves calculating the wave field in the spectral domain by marching along the x-direction. However, $F_n(\nu^2\phi^+)$ in the last term of the above equation should be calculated in the real domain, so, at each step, recourse to the real domain by the inverse FFT is needed.

Equation (19) represents N first-order ordinary differential equations in x, which can be solved by a fourth-order Runge–Kutta method. The finite-difference expression of the Runge–Kutta method used in this study to solve $\hat{\phi}_x^+ = f(x, \hat{\phi}^+)$ is

$$\hat{\phi}_{i+1}^+ = \hat{\phi}_i^+ + \tfrac{1}{6}(k_1 + 2k_2 + 2k_3 + k_4), \tag{20}$$

$$k_1 = \Delta x f(x, \hat{\phi}_i^+), \quad k_2 = \Delta x f(x + \tfrac{1}{2}\Delta x, \hat{\phi}_i^+ + \tfrac{1}{2}k_1),$$

$$k_3 = \Delta x f(x + \tfrac{1}{2}\Delta x, \hat{\phi}_i^+ + \tfrac{1}{2}k_2), \quad k_4 = \Delta x f(x + \Delta x, \hat{\phi}_i^+ + k_3),$$

in which the subscripts i and $i+1$ denote the values at $x = i\Delta x$ and $x = (i+1)\Delta x$, respectively. In our problem, $f(x, \hat{\phi}^+)$ is the right-hand side of (19). When we calculate k_2, k_3 and k_4, the $F_n(\nu^2\phi^+)$ term is needed from the real domain. For example, using the half-step central difference for $[\bar{k}^2 - (n\lambda)^2]_x^{\frac{1}{2}}$, k_2 is calculated by

$$\begin{aligned} k_2 = {} & \mathrm{i}\Delta x[\bar{k}^2(x + \tfrac{1}{2}\Delta x) - (n\lambda)^2]^{\frac{1}{2}}(\hat{\phi}_i^+ + \tfrac{1}{2}k_1) \\ & - \frac{[\bar{k}^2(x+\Delta x) - (n\lambda)^2]^{\frac{1}{2}} - [\bar{k}^2(x) - (n\lambda)^2]^{\frac{1}{2}}}{2[\bar{k}^2(x + \frac{1}{2}\Delta x) - (n\lambda)^2]^{\frac{1}{2}}}(\hat{\phi}_i^+ + \tfrac{1}{2}k_1) \\ & - \frac{\mathrm{i}\Delta x \bar{k}^2(x + \frac{1}{2}\Delta x)}{2[\bar{k}^2(x + \frac{1}{2}\Delta x) - (n\lambda)^2]^{\frac{1}{2}}} F_n[\nu^2(x + \tfrac{1}{2}\Delta x, y)\, F^{-1}(\hat{\phi}_i^+ + \tfrac{1}{2}k_1)]. \end{aligned}$$

As can be seen in (20), in the Runge–Kutta method used in this study, depth information at every $\frac{1}{2}\Delta x$ is needed to calculate the wave field at every Δx. Thus we need the computation of four FFT's and four inverse-FFT's at each step.

In the discrete propagation model (19), the wave modes for which $(n\lambda)^2 \geqslant \bar{k}^2$ are evanescent. Since in general $\bar{k}$ has the minimum value at the offshore boundary, some evanescent modes become progressive modes as they propagate into shallower region. In this study these evanescent modes are neglected and only the progressive modes at the offshore boundary are carried into the domain. For straight and parallel contours, this can be justified on the basis that the newly arising progressive modes represent the trapped wave modes that cannot be excited from offshore.

For the purpose of the stability analysis of the numerical method described above, first we consider the following simplified equation:

$$\hat{\phi}_x^+ = \mathrm{i}\tilde{k}\hat{\phi}^+, \tag{21}$$

where $\tilde{k} = [\bar{k}^2 - (n\lambda)^2]^{\frac{1}{2}}$, which is real or imaginary depending on the relative magnitudes of $\bar{k}^2$ and $(n\lambda)^2$. Here we consider only the progressive modes for which $\tilde{k}$ is real. The above equation is approximated in the Runge–Kutta method by

$$\hat{\phi}^+(x + \Delta x) = [1 + \mathrm{i}\tilde{k}\Delta x - \tfrac{1}{2}(\tilde{k}\Delta x)^2 - \tfrac{1}{6}\mathrm{i}(\tilde{k}\Delta x)^3 + \tfrac{1}{24}(\tilde{k}\Delta x)^4]\hat{\phi}^+(x), \tag{22}$$

where we assumed $\tilde{k}$ to be constant for simplicity of analysis. We use one-dimensional (in x) von Neumann stability analysis to determine the condition that has to be imposed on the step size Δx. We look for a solution to (22) of the form

$$\hat{\phi}^+(x) = \xi^{x/\Delta x},$$

where ξ is the amplification factor and we need $|\xi| \leqslant 1$ for stability. Substitution in (22) gives

$$|\xi| = \left[1 - \frac{(\tilde{k}\Delta x)^6}{72} + \frac{(\tilde{k}\Delta x)^8}{576}\right]^{\frac{1}{2}}. \tag{23}$$

The above equation in plotted in figure 1 for varying $\tilde{k}\Delta x$. The solution becomes

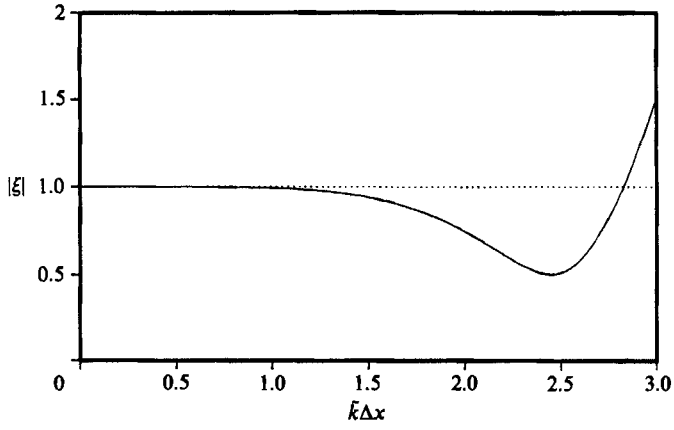

FIGURE 1. Amplification factor $|\xi|$ as a function of $\tilde{k}\Delta x$ in the fourth-order Runge–Kutta method to solve $\hat{\phi}_x^+ = \mathrm{i}\tilde{k}\hat{\phi}^+$.

unstable if $\tilde{k}\Delta x > 2.828$ and shows severe damping in the range $1.5 \leqslant \tilde{k}\Delta x \leqslant 2.8$. Therefore, for the solution to be accurate as well as stable ($0.99 \leqslant |\xi| \leqslant 1.0$), we need

$$\Delta x[\bar{k}^2 - (n\lambda)^2]^{\frac{1}{2}} \leqslant 1.09. \tag{24}$$

$|n\lambda|$ varies from 0 to $\pi/\Delta y$. Thus from (24) we obtain

$$\Delta x \leqslant \frac{1.09}{\bar{k}_{\max}}. \tag{25}$$

Note that there is no restriction on choosing Δy unless the evanescent modes are included in the computation.

In the above stability analysis, the second and the third terms on the right-hand side of (19) were neglected, which should be important for the numerical stability in cases of steep bottom slopes or large lateral depth variation, respectively. Consider now a problem with just the refraction/shoaling term alone:

$$\hat{\phi}_x^+ = -\hat{k}\hat{\phi}^+, \tag{26}$$

where

$$\hat{k} = \frac{[\bar{k}^2 - (n\lambda)^2]_x^{\frac{1}{2}}}{2[\bar{k}^2 - (n\lambda)^2]^{\frac{1}{2}}} \tag{27}$$

which is always positive for the progressive modes propagating on the beach with decreasing depth in the positive x-direction. Again assuming $\hat{k}$ to be constant over the distance of several Δx and following a procedure similar to the above, we get

$$|\xi| = |1 - \hat{k}\Delta x + \tfrac{1}{2}(\hat{k}\Delta x)^2 - \tfrac{1}{6}(\hat{k}\Delta x)^3 + \tfrac{1}{24}(\hat{k}\Delta x)^4|. \tag{28}$$

For positive $\hat{k}\Delta x$, $|\xi|$ starting from 1 at $\hat{k}\Delta x = 0$ decreases to about 0.27 at $\hat{k}\Delta x = 1.6$ and increases monotonically after that. Again to satisfy the condition for stable and accurate solution, $0.99 \leqslant |\xi| \leqslant 1.0$, we need

$$\Delta x \leqslant \frac{0.02[\bar{k}^2 - (n\lambda)^2]^{\frac{1}{2}}}{[\bar{k}^2 - (n\lambda)^2]_x^{\frac{1}{2}}}. \tag{29}$$

This condition states that we need smaller Δx for a steeper beach slope.

For the wave–bottom interaction term (the last term in (19)), for simplicity of analysis we assume ν^2 to be constant and consider the following problem:

$$\hat{\phi}^+ = -\mathrm{i}\check{k}\hat{\phi}^+, \tag{30}$$

where

$$\check{k} = \frac{\bar{k}^2\nu^2}{2[\bar{k}^2-(n\lambda)^2]^{\frac{1}{2}}}. \tag{31}$$

Again assuming $\check{k}$ to be constant over a short distance in the x-direction and following the above procedure, we get

$$\Delta x \leqslant \frac{2.18[\bar{k}^2-(n\lambda)^2]^{\frac{1}{2}}}{\bar{k}^2|\nu^2|}. \tag{32}$$

This condition states that we need smaller Δx as the bottom topography deviates largely from straight and parallel contours.

In the actual computation, Δx is determined so as to satisfy (25), and the conditions (29) and (32) are monitored during the computation.

4. Incorporation of nonlinearity

To date several approaches have been used to incorporate nonlinearity in the water wave propagation models. One approach is to modify a linear model by the inclusion of a cubic (in amplitude) nonlinear term which represents the distortion of the phase speed resulting from third-order effects in the Stokes theory (see Yue & Mei 1980; Kirby & Dalrymple 1983; Liu & Tsay 1984). This approach has the advantage of having an analytic foundation, but it has a distinct disadvantage in that it becomes invalid in the limit of shallow water. The second approach is to use a basic linear model with an empirical dispersion relation which models amplitude dispersion in shallow water and becomes asymptotic to the linear dispersion relation in deep water (see Booji 1981). Thus this approach leads to the prediction of erroneous wave parameters in the deep-water limit.

Considering these drawbacks of the above approaches, Kirby & Dalrymple (1986) have proposed an empirical dispersion relation which smoothly matches the Hedges' (1976) approximate shallow-water dispersion relation to the analytic results for Stokes waves in intermediate and deep water:

$$\omega^2 = gk[1+f_1(kh)\,\epsilon^2 D]\tanh[kh+f_2(kh)\,\epsilon], \tag{33}$$

where $\epsilon = ka$; a is the wave amplitude from the linear theory, and

$$f_1(kh) = \tanh^5 kh,$$
$$f_2(kh) = [kh/\sinh kh]^4,$$
$$D = \frac{\cosh 4kh + 8 - 2\tanh^2 kh}{8\sinh^4 kh}.$$

This nonlinear dispersion relation may be used in modelling efforts in two ways as discussed by Kirby & Dalrymple (1986). First, the dispersion relation may be incorporated directly in the mild-slope equation. In the present study, we use the second method, which consists of using (33) to correct iteratively the wave parameters in the linear model. First, we perform the computation with the wave parameters given by the linear dispersion relation (3). Then the local wave

parameters are corrected by the nonlinear dispersion relation (33) using the local wave amplitudes calculated previously. The model computation is then performed again, with the corrected wave parameters. This procedure is repeated until the corrected wave parameters yield little difference from the previous ones. In the numerical examples described in the following sections, the iteration was continued until the corrected wavenumber lay within $\pm 1\%$ of the previous value at every grid point.

When we use the fourth-order Runge–Kutta method to solve (19), wave amplitudes are computed at main grid points spaced by Δx from $x = 0$, with the corrected wave parameters at those points. However, the wave parameters at the auxiliary grid points spaced by Δx from $x = -\frac{1}{2}\Delta x$ also should be corrected, but the wave amplitudes are not computed at these points. Thus, the wave amplitudes at the auxiliary grid points are interpolated by a cubic spline in the x-direction using those at the main grid points.

5. Interaction between surface wave and bottom topography

The term $F_n(\nu^2\phi^+)$ in (19) represents the interaction between the directional wave modes and the lateral bottom variation, which can force the evolution of the various directional modes, even if they are initially of zero magnitude. In order to examine this mechanism, we express $F_n(\nu^2\phi^+)$, in terms of periodic convolution, as

$$F_n(\nu^2\phi^+) = \frac{1}{N}\sum_{m=0}^{N-1} \hat{\nu}^2(x, m\lambda)\,\hat{\phi}^+(x, (n-m)\,\lambda), \tag{34}$$

where $\hat{\nu}^2(x, m\lambda)$, $m = 0$ to $(N-1)$, is the discrete Fourier series obtained by the Fourier transform of $\nu^2(x, y)$ in the y-direction. This equation indicates that the mth bottom mode $\hat{\nu}^2(x, m\lambda)$ coupled with the $(n-m)$th surface wave mode produces or changes the nth wave mode.

In order to illustrate this more explicitly, we have applied the model to a monochromatic wavetrain travelling over a bed whose depth is constant in the x-direction but varies sinusoidally in the y-direction, creating transverse bottom ridges and troughs on the bed. These ridges and troughs begin at $x = 0$. In this particular example, the refraction/shoaling term on the right-hand side in (19) vanishes. The mean water depth is 10 m and the wavelength and amplitude of the bed are 640 m and 2 m, respectively, as shown in figure 2. At $x = 0$, a plane wave of 8 s period and 1 m amplitude enters the domain at an incident angle of 12.8°. We have taken $\Delta x =$ 5 m and $\Delta y = 10$ m to make a grid of 500×128 rows over the 2500×1280 m model area, so that the wave mode at $x = 0$, $\hat{\phi}^+(0, n\lambda)$, is non-zero for $n = 4$ and zero for all other modes, while the bottom modes $\hat{\nu}^2(x, m\lambda)$ are appreciable for $m = 2, 4, 6, N-6$, $N-4, N-2$ and are negligibly small for all other modes as shown in figure 3. At the first step, these bottom modes interact with $\hat{\phi}^+(0, 4\lambda)$ and generate the wave modes of $n = 6, 8, 10, -2, 0, 2$, respectively, which were initially of zero magnitude. Note that in an FFT, the following changes are made: $\hat{\nu}^2(x, (N-m)\,\lambda) = \hat{\nu}^2(x, -m\lambda)$. The mechanism for the subsequent generation of new directional modes is very complicated. Note that only the even-number modes are generated in this particular example.

Figure 4 (*a–d*) shows the amplitude spectra of the progressive modes at different sections. The wave field at $x = 0$ (figure 4*a*) is described by single wave mode, $\hat{\phi}^+(0, 4\lambda)$, which is propagating at 12.8° to the x-axis. The growth of new modes near the initial condition is shown in figure 4 (*b, c*), and the broad spectrum at $x =$

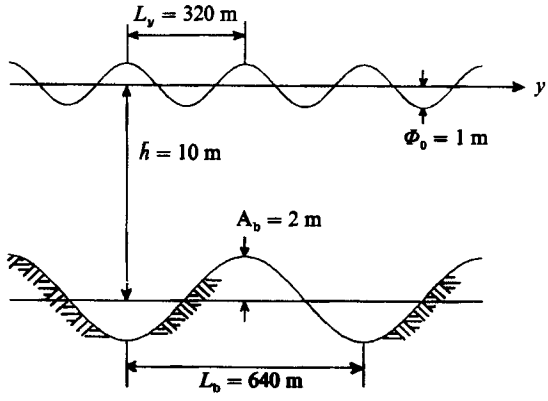

FIGURE 2. Bottom geometry and the initial condition of the wave field for the example of wave propagation over a bathymetry consisting of periodic ridges and troughs. $T = 8$ s, $\theta_0 = 12.8°$, at $x = 0$.

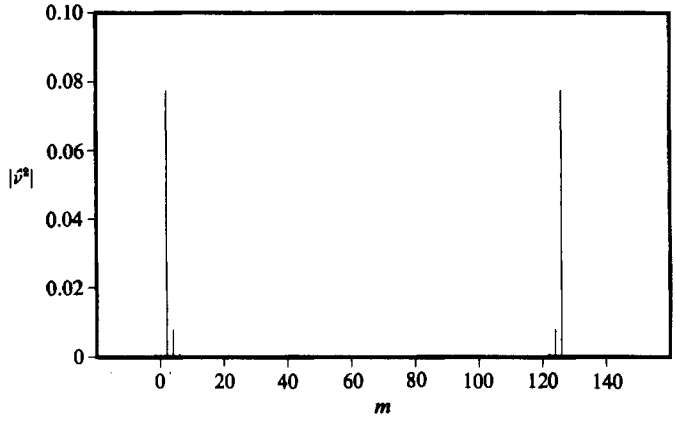

FIGURE 3. Amplitude spectrum of the bottom modes $\hat{\nu}^2(x, m\lambda)$ for the periodic bathymetry shown in figure 2. Note that $\hat{\nu}^2(x, m\lambda)$ is different from the depth $\hat{h}(x, m\lambda)$ which gives non-zero values for $m = 2$ and $N-2$ and zero for all other values of m.

2500 m is shown in figure 4(*d*). Again observe that the odd-number modes are never generated in the linear model.

Another interesting result in this example is the wave trapping over the ridge as shown in figure 5, which is the contour map of the instantaneous free-surface elevation at intervals of 0.5 m. The waves passing over the central ridge are focused near $x = 700$ m, $y = 720$ m and turn back to the left. Mei (1983) has discussed this problem based on ray theory. Some of the rays determined by the Mei's method are drawn in figure 5. The rays 1, 2 and 8, counting from the left, travel over the wavy bed without being trapped. The rays 3 to 7, however, are trapped. For these rays computation was stopped at the turning points, where the ray model blows up, but the extrapolation of these rays can explain the wave trapping phenomenon over the ridge in this example.

6. Verification of the model for irregular bathymetry

For the purpose of testing the model for the prediction of wave deformation on an irregular bathymetry, we have chosen the experiment reported by Berkhoff, Booij &

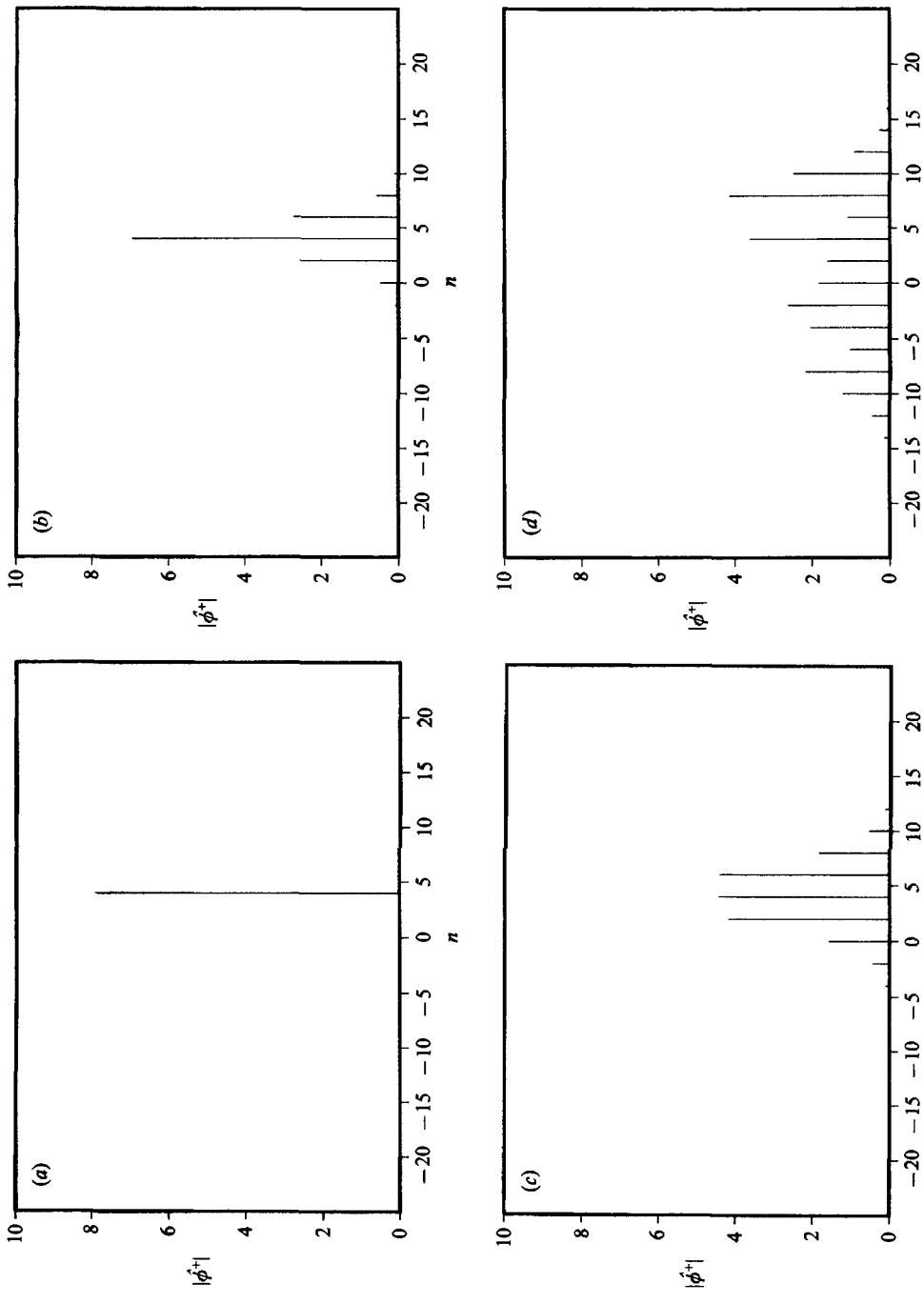

FIGURE 4. Evolution of the amplitude spectra of the progressive modes at different sections for the example illustrated in figure 2. (*a*) $x = 0$ m, (*b*) 100 m, (*c*) 200 m, (*d*) 2500 m.

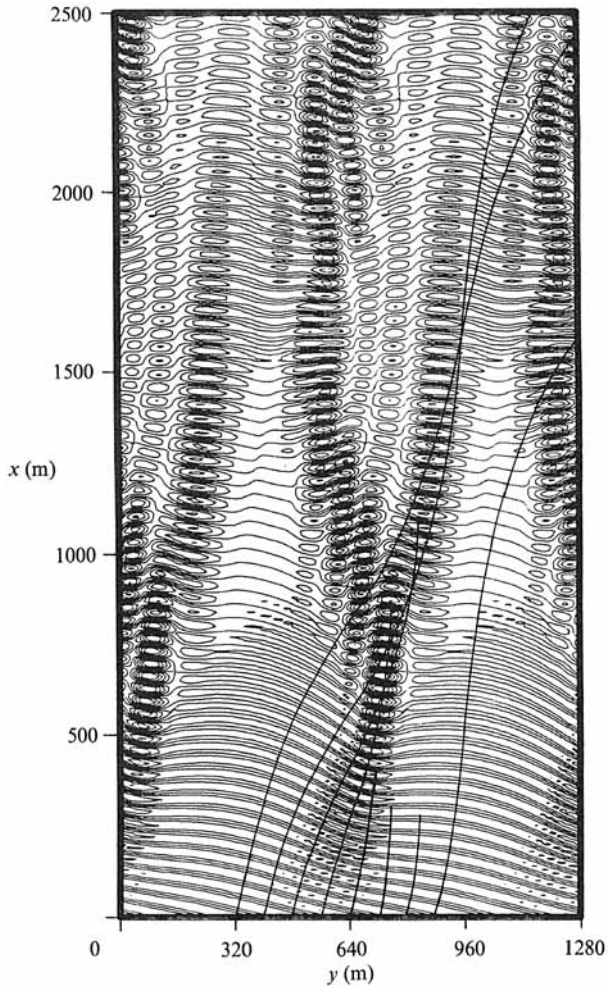

FIGURE 5. Instantaneous wave field over periodic ridges and troughs shown in figure 2. The lines denote wave rays, emanating from $x = 0$ at 12.8° angle of incidence at intervals of 80 m.

Radder (1982). The experimental conditions satisfy most of the assumptions made in the present model, which are mildly varying bathymetry and negligible currents and wave reflection. The periodic lateral boundary condition is not met, but, as will be seen below, the model predicts the wave field reasonably well over the entire vicinity of a refractive focus where diffractive and nonlinear effects both become significant, thus indicating that in this region the effect of the lateral boundaries is not significant with the chosen computational domain.

The experimental bathymetry consists of an elliptic shoal situating on a plane sloping beach with a slope 1:50. The slope rises from a region of constant depth $h =$ 0.45 m, and the entire slope is rotated clockwise at an angle of 20° from a straight wave paddle. Bottom contours (solid lines) in the chosen computational domain are shown in figure 6 along with the labelled transects 1–8 (dashed lines) for which data from the laboratory experiment of Berkhoff *et al.* are available. The offshore boundary of the computational domain is chosen so that water depth is constant

along $x = 0$. The initial condition for the wave then corresponds to the uniform wavetrain generated by the wave paddle, i.e.,

$$\Phi(x = 0, y) = \Phi_0,$$

where $\Phi_0 = 0.0232$ m, which also corresponds to the amplitude of the incident wave. The wave period $T = 1$ s.

In order to describe the geometry of the shoal, we introduce slope-oriented coordinates (x', y') as in figure 6, which are related to the computational coordinates (x, y) by

$$x' = (x-10.5)\cos 20° + (y-10)\sin 20°,$$

$$y' = (x-10.5)\sin 20° - (y-10)\cos 20°.$$

The origin $(x', y') = (0, 0)$ corresponds to the centre of the shoal. Then the water depths in the absence of the shoal are described by

$$h = \begin{cases} h_0 = 0.45 \text{ m}, & x' < -5.84 \text{ m}, \\ h_0 - 0.02(5.84 + x') \text{ m}, & x' \geqslant -5.84 \text{ m}. \end{cases}$$

The boundary of the shoal is given by

$$(\tfrac{1}{3}x')^2 + (\tfrac{1}{4}y')^2 = 1$$

and the depth in the shoal region is modified according to

$$h = h + 0.3 - 0.5[1 - (\tfrac{1}{3.75}x')^2 - (\tfrac{1}{5}y')^2]^{\frac{1}{2}},$$

resulting in a depth at the centre of the shoal of 0.1332 m.

In the computational domain we have chosen, $\bar{k}_{\max} = 5.827$ m^{-1}, which occurs at $x = 20$ m. To satisfy the condition (25) for stable and accurate solutions, we have taken $\Delta x = 0.1$ m and $\Delta y = 0.3125$ m to make a grid of 201×64 rows. Computations were made using both the linear model and the nonlinear version which utilizes the nonlinear dispersion relation (33) to iteratively correct wave parameters. Comparison with the measurements along the transects 1–8 are shown in figure 7(*a–h*) in terms of normalized wave amplitude with respect to the incident wave amplitude. In each figure, nonlinear and linear model results are indicated by solid and dashed lines, respectively, while open circles indicate measured data points. The results of a nonlinear parabolic model (i.e. Kirby & Dalrymple 1983) are also shown as dotted lines. Note that for the transects 1–5 the lateral direction in this paper is flipped compared with the figures presented in Berkhoff *et al.* (1982). Since the transects 6 and 8 do not correspond to any of our grid lines, the wave amplitudes along these transects were interpolated using a cubic spline in the y-direction. Taken as a whole, the inclusion of the nonlinear dispersion relation improves the model results greatly, especially in the vicinity of a refractive focus where the amplitude dispersion plays an important role.

As shown in figure 7, the results of our nonlinear model are comparable with those of the nonlinear parabolic model. In order to give a more quantitative comparison between the numerical models and the measurements, we have employed the statistical procedure proposed by Willmott (1981). He criticizes the traditional statistical measures such as the correlation coefficient, its square and their statistical significance for evaluating the errors of model predictions (P) against observations (O).

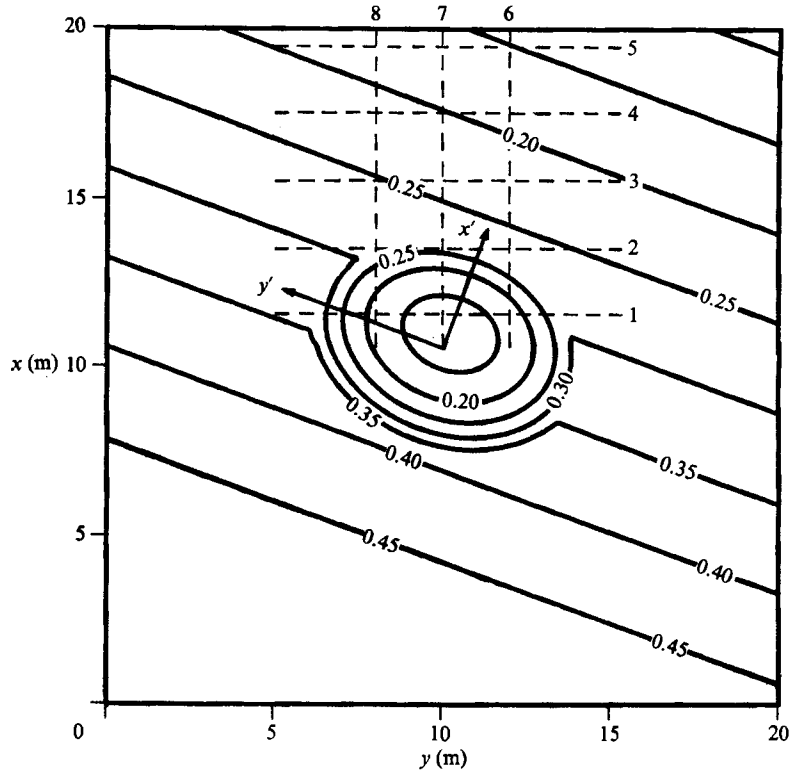

FIGURE 6. Bathymetry of the computational domain for the experiment by Berkhoff *et al.* (1982). Dashed lines indicate the transects of wave measurement.

As alternative measures of error, he proposes the root-mean-squared error

$$\mathrm{RMSE} = \left[\frac{1}{N}\sum_{i=1}^{N}(P_i - O_i)^2\right]^{\frac{1}{2}} \tag{35}$$

and its systematic and unsystematic parts in order to give pertinent information about the nature of the error

$$\mathrm{RMSE_s} = \left[\frac{1}{N}\sum_{i=1}^{N}(\hat{P}_i - O_i)^2\right]^{\frac{1}{2}}, \quad \mathrm{RMSE_u} = \left[\frac{1}{N}\sum_{i=1}^{N}(P_i - \hat{P}_i)^2\right]^{\frac{1}{2}}, \tag{36}$$

where $\hat{P}_i = a + bO_i$, and a and b are the intercept and the slope obtained from an ordinary least-square analysis between O and P. They satisfy the following relation:

$$\mathrm{RMSE}^2 = \mathrm{RMSE_s^2} + \mathrm{RMSE_u^2}. \tag{37}$$

Willmott suggests that if RMSE is largely composed of $\mathrm{RMSE_s}$, further refinement of the model is needed in the direction to minimize $\mathrm{RMSE_s}$ in order that the model predicts at its maximum possible accuracy, but on the other hand, if $\mathrm{RMSE_u}$ is the major portion of RMSE, perhaps the model is as good as it is without major reworking.

As a measure of the degree to which a model's predictions are error free but not

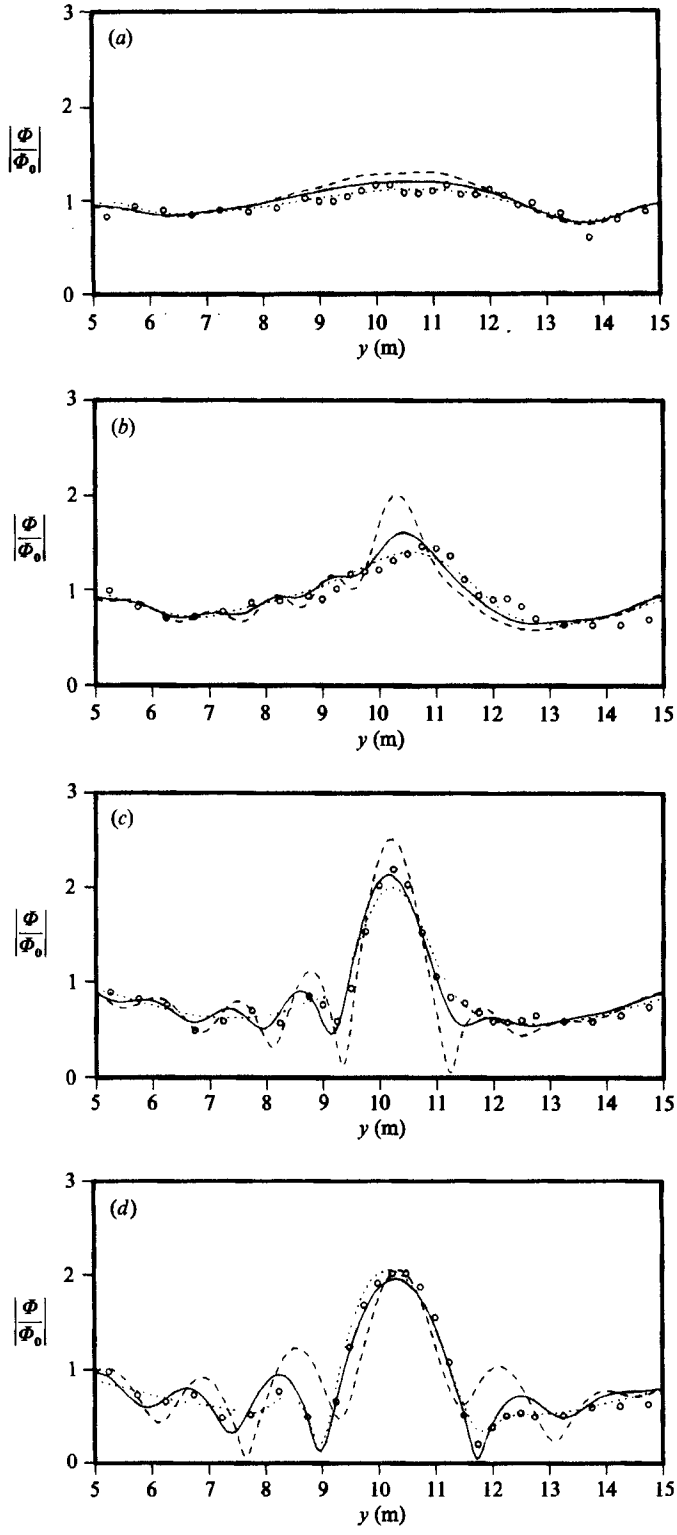

FIGURE 7 (*a–d*). For caption see facing page.

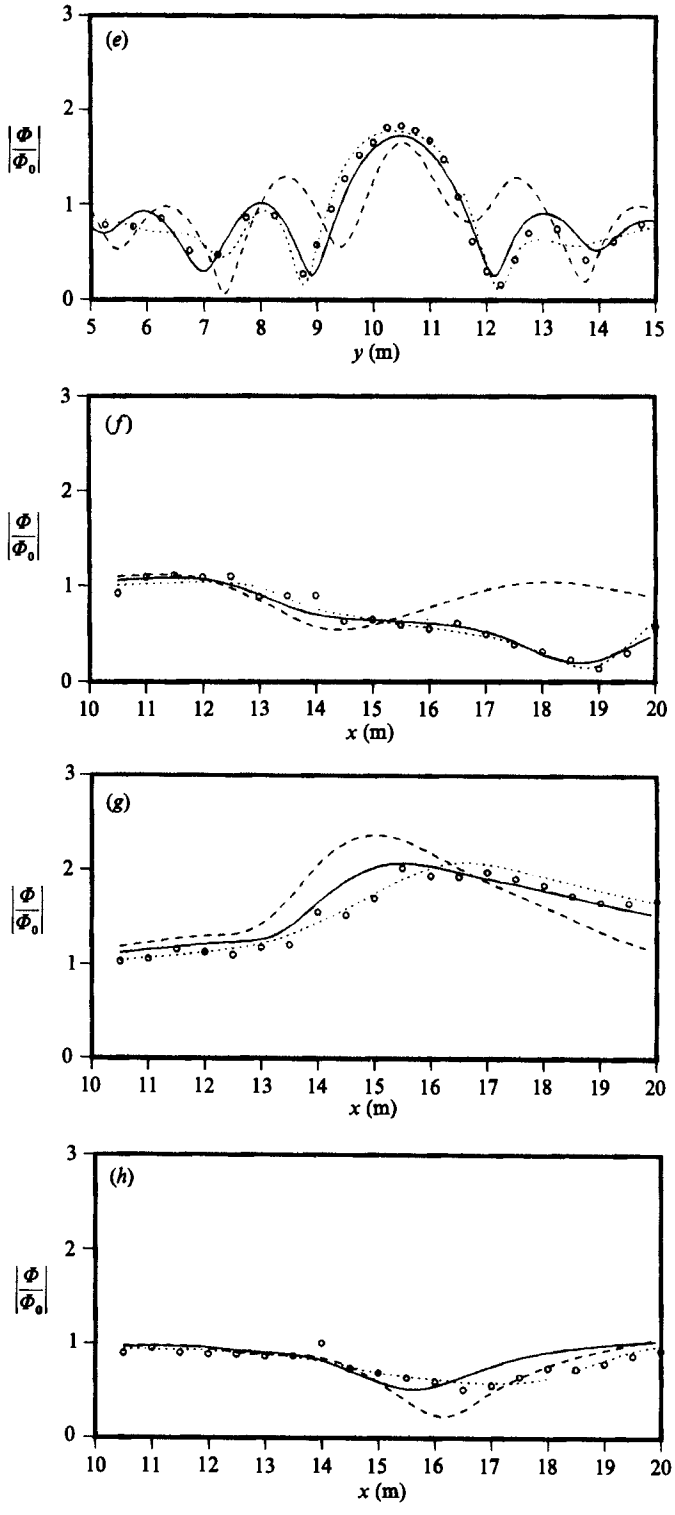

FIGURE 7. Comparison of the model results against the experimental data by Berkhoff *et al.* (1982) in terms of normalized wave amplitude with respect to incident amplitude: ○, experiment; ---, linear model; ——, nonlinear model; ....., nonlinear parabolic model. (*a*)–(*h*) sections 1–8 (see figure 6) respectively.

Section no.	N	RMSE (cm)	$RMSE_u$ (cm)	$RMSE_s$ (cm)	d
1	28	0.168 (0.138)	0.142 (0.103)	0.090 (0.092)	0.923 (0.928)
2	28	0.283 (0.189)	0.283 (0.180)	0.019 (0.055)	0.945 (0.973)
3	28	0.256 (0.271)	0.250 (0.240)	0.055 (0.126)	0.986 (0.983)
4	27	0.229 (0.205)	0.186 (0.193)	0.133 (0.068)	0.991 (0.993)
5	28	0.301 (0.237)	0.236 (0.234)	0.186 (0.041)	0.980 (0.990)
6	20	0.191 (0.148)	0.175 (0.137)	0.078 (0.057)	0.981 (0.988)
7	20	0.302 (0.197)	0.253 (0.166)	0.164 (0.105)	0.962 (0.985)
8	20	0.292 (0.139)	0.255 (0.135)	0.144 (0.032)	0.799 (0.951)
Total	199	0.256 (0.199)	0.248 (0.195)	0.063 (0.043)	0.983 (0.990)

TABLE 1. Statistical parameters for evaluating the errors of numerical models against measurements for the experiment by Berkhoff *et al.* (1982) (following Willmott's 1981 procedure). The values in parentheses indicate the results from the nonlinear parabolic model of Kirby & Dalrymple (1983).

a measure of correlation or association between the observed and predicted variates, Willmott introduces a dimensionless quantity, d, as an index of agreement

$$d = 1 - \frac{\sum_{i=1}^{N} (P_i - O_i)^2}{\sum_{i=1}^{N} [|P_i - \bar{O}| + |O_i - \bar{O}|]^2}, \tag{38}$$

where $\bar{O}$ is the mean of the observed variates. The values for d vary between 0 and 1.0, where 1.0 indicates perfect agreement between observations and predictions, and 0 connotes complete disagreement.

These statistical parameters computed for each transect in figure 6 and for total measurement points are summarized in table 1, in which the values in parentheses indicate the result from the nonlinear parabolic model. For most of the cases, $RMSE_s$ is very small compared with RMSE, indicating that these models hardly need further refinement. Except for the transect 8, the values of d do not show a big difference between the two models and are close to 1.0, indicating that our model is as good as the parabolic one. The slightly worse agreement of the present model than the parabolic model along the transect 8 could be caused by the intrusion of the boundary effects since the wave on the slope refracts towards the right.

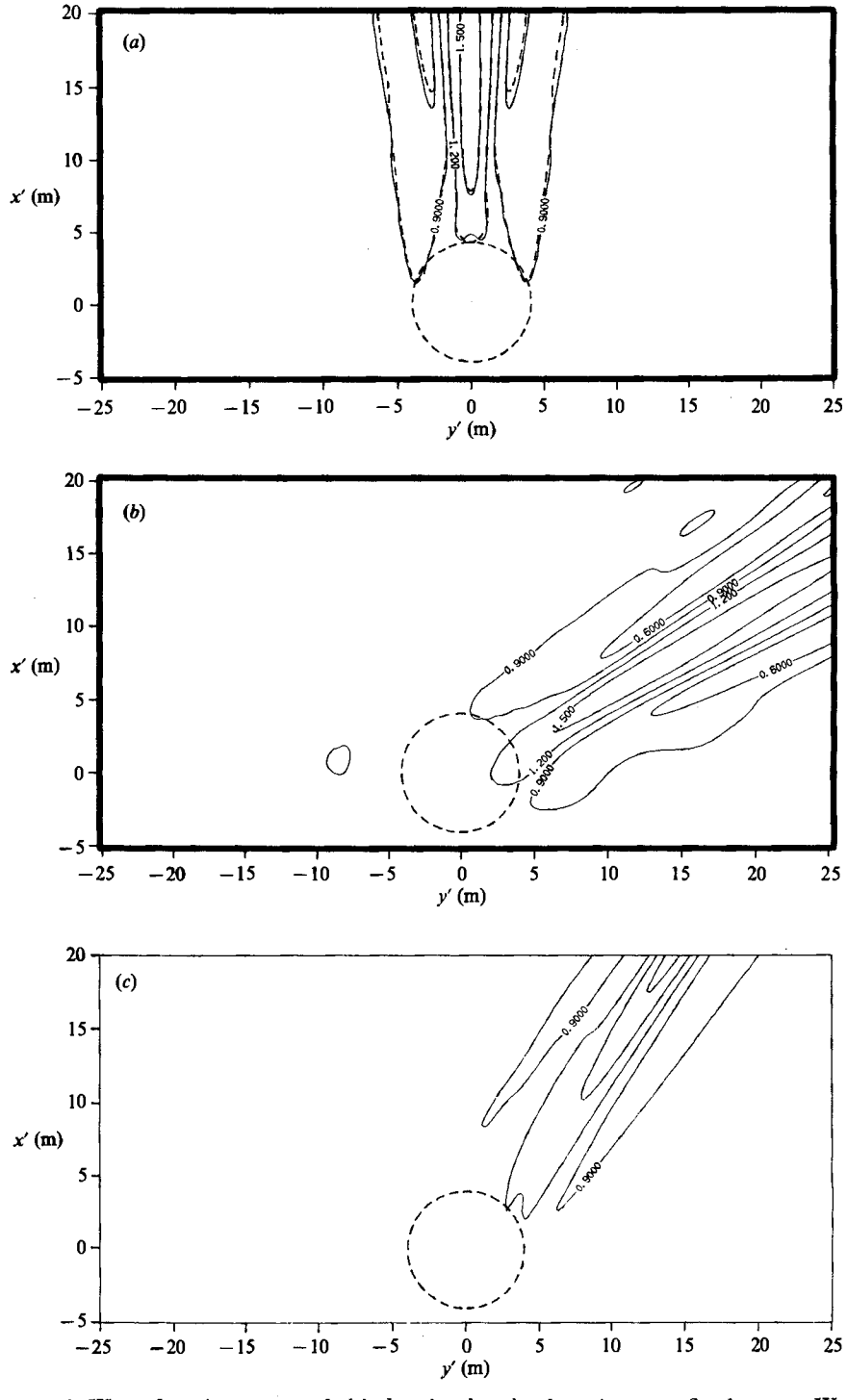

FIGURE 8. Wave focusing pattern behind a circular shoal resting on a flat bottom. Water depth is given by (39) with $\alpha = 0.12, \beta = 0.2$. Contours are at intervals of 0.3 for normalized wave amplitude with respect to incident amplitude. (*a*) $\theta_0 = 0°$ (——, present model; – – –, parabolic model); (*b*) $\theta_0 = 60°$ (present model); (*c*) $\theta_0 = 60°$ (parabolic model).

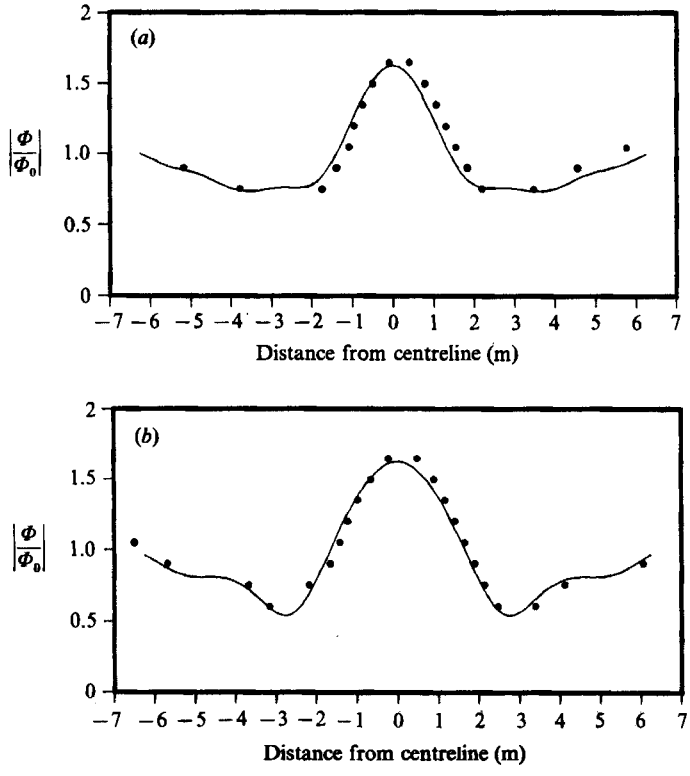

FIGURE 9. Comparison of the model results of $\theta_0 = 60°$ (black dots) against those of normal incidence (——) in terms of normalized wave amplitude with respect to incident amplitude at different sections behind the circular shoal illustrated in figure 8. (*a*) $x' = 10$ m, (*b*) $x' = 15$ m.

7. Test of the model for large angle of incidence

Through the above example we have verified that our model is a reasonably good predictor of the wave field development on an irregular bathymetry where the effects of refraction, diffraction and nonlinearity are equally significant. However, that example is not sufficient for showing the applicability of the model to a large angle of incidence. The next example, chosen for this purpose, is for a monochromatic wavetrain focusing behind a circular shoal resting on a flat bottom. Owing to the axisymmetry of the circular shoal, the wave focusing pattern behind the shoal should be independent of the angle of incidence, if the model predicts it 'correctly'. Since the purpose of this example is to test how the model works for large angle of incidence, only the linear model results are presented.

The water depth for the first series of tests is given by

$$h = \begin{cases} h_0, & r > R, \\ h_0 + \alpha - \beta\{1 - [(\frac{1}{5}x')^2 + (\frac{1}{5}y')^2]\}^{\frac{1}{2}}, & r \leqslant R, \end{cases} \tag{39}$$

where $h_0 = 0.336$ m, $\alpha = 0.12$, $\beta = 0.2$, $R = 4$ m is the radius of the shoal, $r = (x'^2 + y'^2)^{\frac{1}{2}}$ and (x', y') are the coordinates with the origin at the crest of the shoal. The shoal height at the crest is 0.08 m. The same wave period and amplitude as those of Berkhoff *et al.* (1982) are used. We have taken $\Delta x = 0.1$ m and $\Delta y = 0.3885$ m to make a grid of 250×256 rows over 25×99.5 m model area. The shoal crest is located at $x = 5$ m, $y = 49.73$ m. In this example, since the bottom variability is

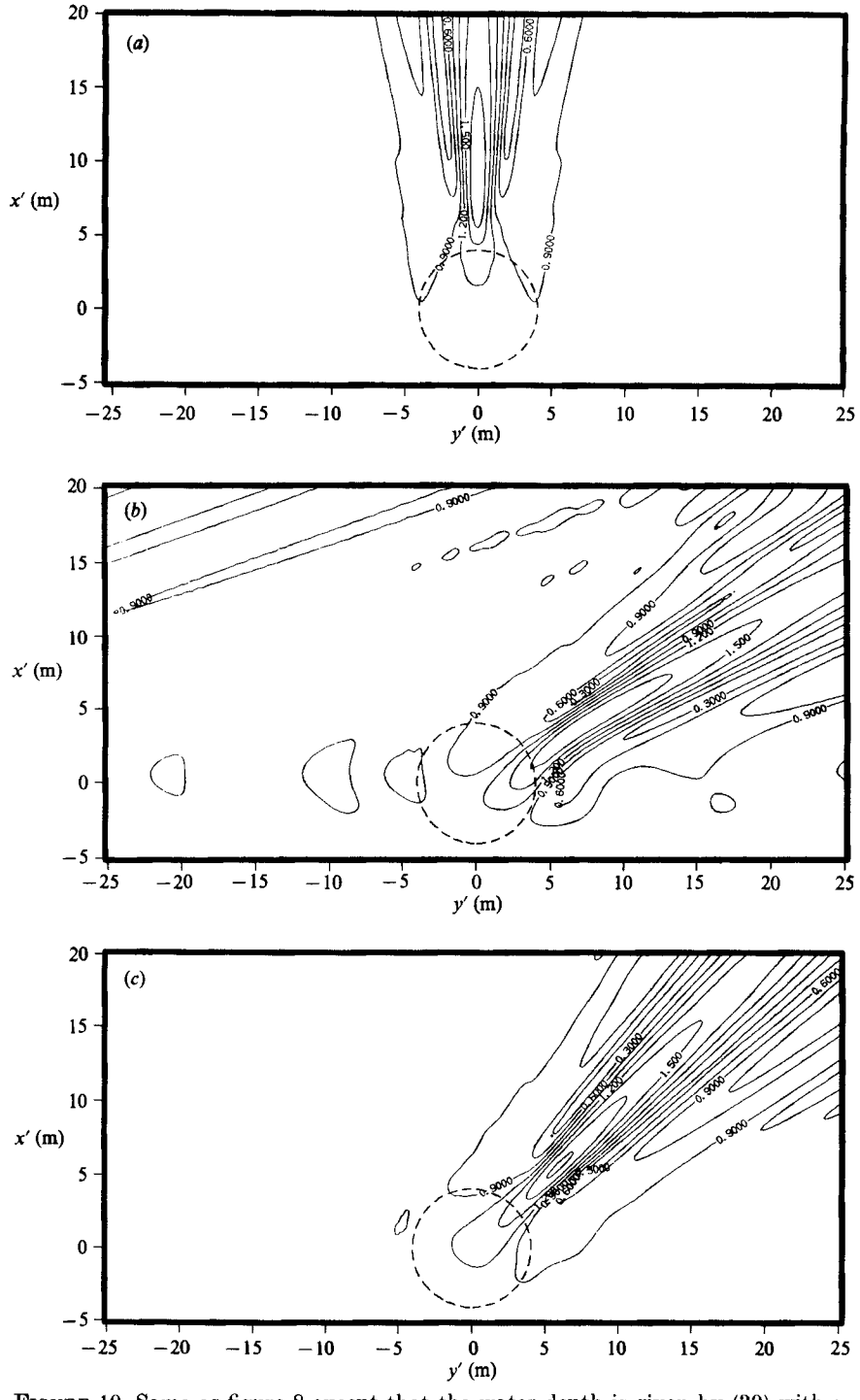

FIGURE 10. Same as figure 8 except that the water depth is given by (39) with $\alpha = 0.18$, $\beta = 0.3$. (*a*) $\theta_0 = 0°$, (*b*) $\theta_0 = 60°$, (*c*) $\theta_0 = 45°$.

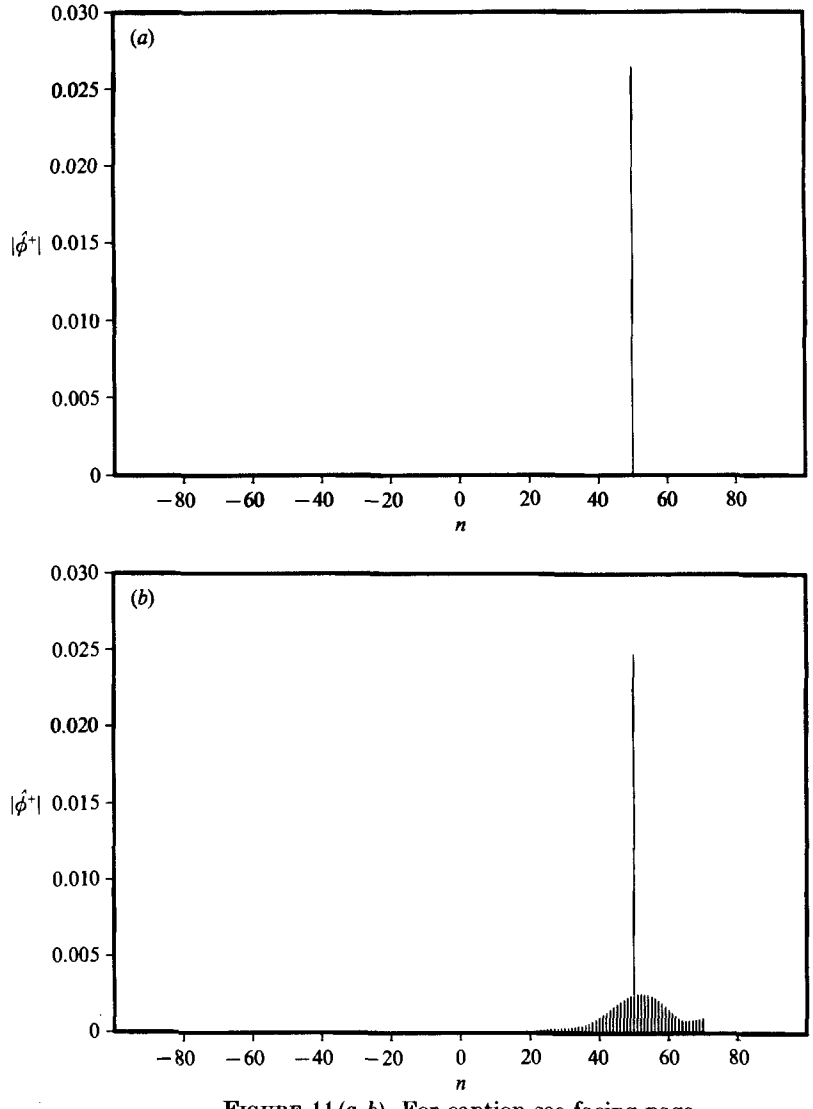

FIGURE 11 (*a*, *b*). For caption see facing page.

confined to the shoal region, k is defined as the wavenumber on the flat bottom so that $\nu^2 = 0$ over the flat bottom region.

Two incident wave angles are tested: $\theta_0 = 0°$ and $\theta_0 = 60°$. The contours of the normalized amplitude with respect to the incident wave amplitude are shown in figure 8 (*a*, *b*) for each incident angle. For brevity only one half of the model area in the y-direction centred the shoal is presented. The results of the linear parabolic model are also shown in figure 8 (*a*) as dashed lines for $\theta_0 = 0°$ and in figure 8 (*c*) for $\theta_0 = 60°$. The difference between the present model and the parabolic one is not significant for $\theta_0 = 0°$. For $\theta_0 = 60°$, however, the parabolic model gives large distortion of the wave focusing pattern. In particular, the centreline of wave focusing rotates by about 25° towards the positive x-direction. For the present model, the asymmetric distortion to the focusing pattern at $\theta_0 = 60°$ is apparent near the shoal. However, the overall wave focusing pattern behind the shoal at $\theta_0 = 60°$

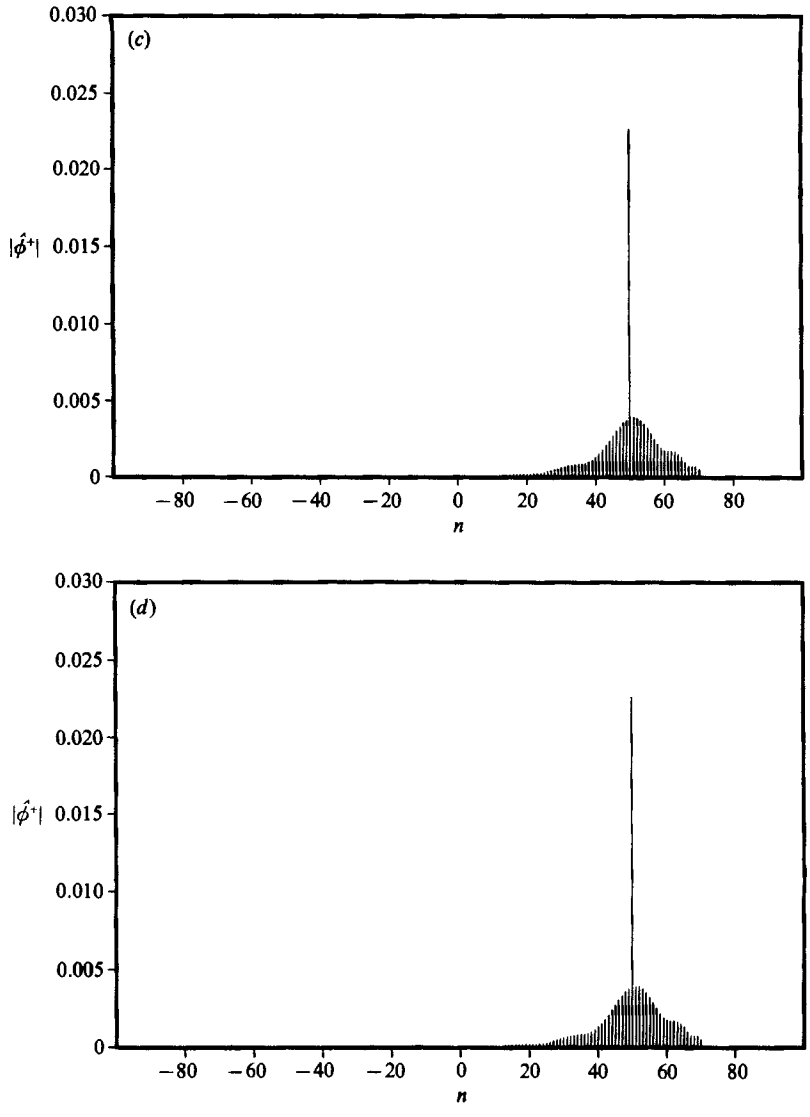

FIGURE 11. Amplitude spectra of the progressive modes at different sections from circular shoal example in figure 10(*c*). (*a*) $x' = -4$ m, (*b*) 0 m, (*c*) 4 m, (*d*) 15 m.

is very similar to that at $\theta_0 = 0°$. For more quantitative comparison between $\theta_0 = 0°$ and $\theta_0 = 60°$ for the present model, the variation of the normalized amplitude along two transects which are 10 m and 15 m from the shoal crest is plotted in figures 9(*a*) and 9(*b*), respectively. The values at $\theta_0 = 0°$ is indicated by solid lines, while the black dots indicate the values at $\theta_0 = 60°$ which were obtained by digitization from a contour map similar to figure 8(*b*) but with higher resolution. The values at $\theta_0 = 60°$ are slightly shifted to the right compared with those at $\theta_0 = 0°$ but the agreement is quite satisfactory, showing that the present model works reasonably well for a large angle of incidence.

The height of the shoal crest in the above test is about $\frac{1}{4}$ of the water depth on the flat bottom. In order to examine the effects of the magnitude of the bottom variation, we have tested the model for a shallower shoal. The water depth for this

series of tests is given by (39) with $\alpha = 0.18$, $\beta = 0.3$ so that the shoal height at the crest is 0.12 m which is about $\frac{1}{3}$ of the water depth on the flat bottom. Figures 10(*a*) and 10(*b*) show the wave amplitude variation at $\theta_0 = 0°$ and $\theta_0 = 60°$, respectively, for the higher shoal. The asymmetric distortion to the focusing pattern at the 60° angle of incidence becomes severe, and the wave amplitude near the centreline of the focusing tends to be overpredicted. Figure 10(*c*) shows the wave amplitude variation at $\theta_0 = 45°$. There is still some apparent asymmetric distortion; however it is much less prominent than that at $\theta_0 = 60°$. The result is that the bigger the bottom variation, the bigger the error of the model for the same angle of incidence.

In Dalrymple & Kirby (1988), it was shown that, on straight and parallel bottom contours, the diffraction pattern behind a breakwater, for example, is determined by the summation of angularly spreading waves. The amplitudes and phases of these waves are dictated by the initial condition imposed at the breakwater, and each wave propagates in the x-direction only undergoing refraction and shoaling. The diffraction is accounted for solely by the initial condition. In this study, the diffraction occurs within the model domain owing to the presence of the shoal. Figure 11(*a–d*) shows the amplitude spectra of the progressive modes at different sections for the example in figure 10(*c*). The wave field just before the shoal (figure 11*a*) is described by one wavetrain, $\phi^+(x, 50\lambda)$, which is propagating at 45° to the x-axis. At the section crossing the shoal crest ($x' = 0$ m), the convolution term, which imposes the interaction of the bottom variation with the wave field, generates additional wavelets, as shown in figure 11(*b*). After the shoal on the constant-depth section, these wavelets angularly disperse without any change in magnitude (compare figures 11*c* and 11*d*), giving rise to the wave pattern behind the shoal.

8. Conclusions and discussion

A wide-angle water-wave propagation model on an irregular bathymetry has been developed by using the spectral Fourier method. The wave field at the initial row ($x = 0$) is transformed into the discrete Fourier space and the evolution of each Fourier mode due to bottom variations is calculated by marching along the x-direction; finally, the real wave field is recovered by taking the inverse Fourier transform in the y-direction.

The model depends on the mild-slope assumption for the variation of the bathymetry and does not include the effects of currents and wave reflection. The most significant restriction of the model, in the application to a practical problem, due to the use of a spectral Fourier method which imposes periodic lateral boundary conditions, is that the domain of the model area should be rectangular and should be large enough in the lateral direction to avoid the intrusion of boundary effects into the area of main interest. An alternative method for eliminating the assumption of the periodic lateral boundary conditions could be the Chebyshev collocation method outlined in Canuto *et al.* (1988), which approximates the lateral variation of the wave field by the Chebyshev polynomials rather than by Fourier series.

In the previous section, we have found that the model becomes inaccurate with greater bottom variation for the same angle of incidence. In order to investigate this, we consider a plane wave travelling over water of constant depth, even if this appears to be irrelevant to the bottom variability. We may choose $\bar{k}^2$ as an arbitrary constant so that ν^2 may also be a non-zero constant. The problem in the real domain is

$$\nabla^2\phi + \bar{k}^2(1-\nu^2)\,\phi = 0,$$

with constant $\bar{k}^2$ and ν^2. The general solution is given by

$$\phi = A \exp[\mathrm{i}(\bar{k}^2(1-\nu^2)-\lambda^2)^{\frac{1}{2}}x]\exp(\mathrm{i}\lambda y),$$

so that

$$\phi_x = \mathrm{i}[\bar{k}^2(1-\nu^2)-\lambda^2]^{\frac{1}{2}}\phi, \tag{40}$$

where λ and A are arbitrary constants. The Fourier transform of (40) in the y-direction leads to

$$\hat{\phi}_x = \mathrm{i}(\bar{k}^2-\lambda^2)^{\frac{1}{2}}\left[1-\frac{\bar{k}^2\nu^2}{\bar{k}^2-\lambda^2}\right]^{\frac{1}{2}}\hat{\phi},$$

which can be approximated by

$$\hat{\phi}_x \approx \mathrm{i}(\bar{k}^2-\lambda^2)^{\frac{1}{2}}\left[1-\frac{\bar{k}^2\nu^2}{2(\bar{k}^2-\lambda^2)}\right]\hat{\phi} \tag{41}$$

for *small* $\bar{k}^2\nu^2/(\bar{k}^2-\lambda^2)$.

On the other hand, our model (15) in water of constant depth reduces to

$$\hat{\phi}_x = \mathrm{i}(\bar{k}^2-\lambda^2)^{\frac{1}{2}}\hat{\phi} - \frac{\mathrm{i}\bar{k}^2\nu^2}{2(\bar{k}^2-\lambda^2)^{\frac{1}{2}}}\hat{\phi}, \tag{42}$$

which is equivalent to (41). Thus, our model should be restricted to small $\bar{k}^2\nu^2/(\bar{k}^2-\lambda^2)$. Actually, ν^2 can be either positive or negative, so the restriction of our model to depth variation is described by

$$\frac{|\nu^2|}{\cos^2\theta} \ll 1, \tag{43}$$

where $\cos^2\theta = (\bar{k}^2-\lambda^2)/\bar{k}^2$ was used. In other words, in order for our model to be accurate for a large angle of incidence, the depth variation in the y-direction should be small.

An inevitable problem which is encountered in any wide-angle model that uses a marching solution technique is the upwave propagation of waves. In the circular shoal tests in the previous section, for example, if a very large-incident-angle wavetrain is modelled, the constant-depth region before the shoal ($x' \leqslant -4$ m) should be affected by the presence of the shoal, while this is not detected by the model since the $\hat{\phi}^-$ terms have been neglected.

This work is partly a result of research sponsored by NOAA Office of Sea Grant, Department of Commerce, under Grant No. NA86AADSG040. J.T.K. was partially supported by the Office of Naval Research (Project N-00014-86-K-0790). The last author (J.W.C.) acknowledges the support of the Korea Science and Engineering Foundation. The authors would like to thank Dr M. W. Dingemans for providing the program for the Willmott's analysis and the measurement data of the Berkhoff *et al.*'s experiment. The US Government is authorized to produce and distribute reprints for governmental purposes, notwithstanding any copyright notation that may appear herein.

REFERENCES

Berkhoff, J. C. W. 1972 Computation of combined refraction–diffraction. In *Proc. 13th Intl Conf. Coastal Engng Vancouver*, pp. 471–490. ASCE.

Berkhoff, J. C. W., Booij, N. & Radder, A. C. 1982 Verification of numerical wave propagation models for simple harmonic linear waves. *Coastal Engng* **6**, 255–279.

BOOIJ, N. 1981 Gravity waves on water with non-uniform depth and current. *Rep.* 81–1, Dept. of Civil Eng., Delft Univ. of Tech.

CANUTO, C., HUSSAINI, M. Y., QUARTERONI, A. & ZANG, T. A. 1988 *Spectral Methods in Fluid Dynamics*. Springer. 557 pp.

DALRYMPLE, R. A. & KIRBY, J. T. 1988 Models for very wide-angle water waves and wave diffraction. *J. Fluid Mech.* **192**, 33–50.

DINGEMANS, M. W., STIVE, M. J. F., KUIK, A. J., RADDER, A. C. & BOOIJ, N. 1984 Field and laboratory verification of the wave propagation model CREDIZ. In *Proc. 19th Intl Conf. Coastal Engng, Houston*, pp. 1178–1191. ASCE.

HEDGES, T. S. 1976 An empirical modification to linear wave theory. *Proc. Inst. Civ. Engrs* **61**, 575–579.

KIRBY, J. T. 1986*a* Higher-order approximations in the parabolic equation method for water waves. *J. Geophys. Res.* **91**, 933–952.

KIRBY, J. T. 1986*b* Rational approximations in the parabolic equation method for water waves. *Coastal Engng* **10**, 355–378.

KIRBY, J. T. & DALRYMPLE, R. A. 1983 A parabolic equation for the combined refraction–diffraction of Stokes waves by mildly varying topography. *J. Fluid Mech.* **136**, 453–466.

KIRBY, J. T. & DALRYMPLE, R. A. 1986 An approximate model for nonlinear dispersion in monochromatic wave propagation models. *Coastal Engng* **9**, 545–561.

LIU, P. L.-F. & MEI, C. C. 1976 Water motion on a beach in the presence of a breakwater. 1. Waves. *J. Geophys. Res.* **81**, 3079–3084.

LIU, P. L.-F. & TSAY, T.-K. 1984 Refraction-diffraction model for weakly nonlinear water waves. *J. Fluid Mech.* **141**, 265–274.

MEI, C. C. 1983 *The Applied Dynamics of Ocean Surface Waves*. Wiley-Interscience. 740 pp.

RADDER, A. C. 1979 On the parabolic equation method for water-wave propagation. *J. Fluid Mech.* **95**, 159–176.

STAMNES, J. J., LØVHAUGEN, O., SPJELKAVIK, B., MEI, C. C., LO, E. & YUE, D. K. P. 1983 Nonlinear focusing of surface waves by a lens – theory and experiment. *J. Fluid Mech.* **135**, 71–94.

WILLMOTT, C. J. 1981 On the validation of models. *Phys. Geog.* **2**, 184–194.

YUE, D. K.-P. & MEI, C. C. 1980 Forward diffraction of Stokes waves by a thin wedge. *J. Fluid Mech.* **99**, 33–52.